Mon. Not. R. Astron. Soc. **000**, 000–000 (0000) Printed 26 September 2005 (MN LATEX style file v2.2)

The UKIRT Infrared Deep Sky Survey $ZYJHK$ Photometric System: Passbands and Synthetic Colours

P. C. Hewett,[1] S. J. Warren,[2] S. K. Leggett,[3] S. T. Hodgkin[1]
[1] *Institute of Astronomy, Madingley Road, Cambridge CB3 0HA*
[2] *Blackett Laboratory, Imperial College of Science Technology and Medicine, Prince Consort Rd, London SW7 2AZ*
[3] *United Kingdom Infrared Telescope, Joint Astronomy Centre, 660 North A'ohoku Place, Hilo, HI 96720*

Accepted Received in original form

ABSTRACT

The UKIRT Infrared Deep Sky Survey is a set of five surveys of complementary combinations of area, depth, and Galactic latitude, which began in 2005 May. The surveys use the UKIRT Wide Field Camera (WFCAM), which has a solid angle of 0.21deg^2. Here we introduce and characterise the $ZYJHK$ photometric system of the camera, which covers the wavelength range $0.83 - 2.37\,\mu$m. We synthesise response functions for the 5 passbands, and compute colours in the WFCAM, SDSS and 2MASS bands, for brown dwarfs, stars, galaxies and quasars of different types. We provide a recipe for others to compute colours from their own spectra. Calculations are presented in the Vega system, and the computed offsets to the AB system are provided, as well as colour equations between WFCAM filters and the SDSS and 2MASS passbands. We highlight the opportunities presented by the new Y filter at $0.97 - 1.07\,\mu$m for surveys for hypothetical Y dwarfs (brown dwarfs cooler than T), and for quasars of very–high redshift, $z > 6.4$.

Key words: surveys, infrared: general

1 INTRODUCTION

The UKIRT Infrared Deep Sky Survey (UKIDSS, Lawrence et al., 2006) commenced on 2005 May 13, and is a set of five surveys of complementary combinations of depth and area, employing the wavelength range $0.83 - 2.37\,\mu$m in up to five filters $ZYJHK$, and extending over both high and low Galactic latitude regions of the sky. The new Y band, $0.97 - 1.07\,\mu$m, is introduced in this paper. It is anticipated that the surveys will take seven years to complete. This paper characterises the photometric system of the survey, and presents synthetic colours of a wide variety of sources. The paper is one of a set of five which provide the reference technical documentation for UKIDSS. The other four papers, described below, are Casali et al. (2006), Lawrence et al. (2006), Irwin et al. (2006) and Hambly et al. (2006).

In this paper all quoted magnitudes are on the Vega system. We use the nomenclature Z, Y, J, H, K for magnitudes in the five bands used by UKIDSS, and we use $J2$, $H2$, $K2$ for the bands of the 2Micron All Sky Survey (2MASS, Cutri et al. 2003), and u, g, r, i, z for the bands of the Sloan Digital Sky Survey (SDSS, York et al. 2000). Quoted depths correspond to 5σ significance for a point source.

The survey instrument is the Wide Field Camera (WFCAM) on the United Kingdom Infrared Telescope (UKIRT). A detailed description of the instrument is provided by Casali et al. (2006). The camera has four Rockwell Hawaii-II 2048^2 PACE arrays, with pixel scale $0.4''$, giving a solid angle of 0.21 deg^2 per exposure. At the time of commissioning, 2004 November, the instrument *étendue*[1] of 2.38 m^2 deg^2 was the largest of any near-infrared imager in the world. The Canada France Hawaii Telescope WIRCam instrument (Puget et al. 2004) covers a solid angle of 0.11 deg^2 per exposure giving an *étendue* of 1.22 m^2 deg^2. WFCAM is likely to remain as the near–infrared imager with the largest *étendue* in the world until completion of the near–infrared camera for VISTA (Dalton et al. 2004). Consequently WFCAM provides the opportunity for new wide surveys, to depths substantially deeper than reached by 2MASS. WFCAM is a common–user instrument, but it is anticipated that the majority of WFCAM observing time will be devoted to UKIDSS.

The scope, layout, and broad science goals of the five components of UKIDSS are described by Lawrence et al. (2006). There are three surveys targeting extraGalactic fields. The Large Area Survey (LAS) is a wide, relatively

[1] product of telescope collecting area, and solid angle of instrument field of view, sometimes called *grasp*

shallow survey that will cover $4000\,\mathrm{deg}^2$ from within the footprint of the SDSS, in the four bands $YJHK$. The depth, $K = 18.4$, will be some 3 mag. deeper than 2MASS. The Deep Extragalactic Survey (DXS), is of intermediate depth, $K = 21.0$, and will cover $35\,\mathrm{deg}^2$ in J and K. The deepest survey is the Ultra Deep Survey (UDS), which will cover $0.78\,\mathrm{deg}^2$ in JHK to a depth $K = 23.0$. Then there are two surveys targeting Galactic fields. The Galactic Plane Survey (GPS) will cover some $1800\,\mathrm{deg}^2$, defined by the sections of the Galactic–latitude band $-5^\circ < b < +5^\circ$ that are contained within the Declination limits $-15^\circ < \delta < +60^\circ$. This region will be imaged in JHK to a depth $K = 19.0$. Finally, the Galactic Clusters Survey will image 11 stellar open clusters and star–formation associations, covering $1400\,\mathrm{deg}^2$, in all five bands $ZYJHK$, to a depth $K = 18.7$.

For typical observing programmes, WFCAM will accumulate data at the rate of approximately 1Tb per week. All WFCAM data are processed by an automated pipeline, described by Irwin et al. (2006). The pipeline flat-fields the data, subtracts the counts from the background sky, detects and parameterises objects, and performs the photometric and astrometric calibrations. The reduced frames and catalogues are ingested into the WFCAM Science Archive, described by Hambly et al. (2006). A process of curation results in seamless images and catalogues, matched across bands. Access to the data is through a flexible query tool, which allows SQL commands for sophisticated searches.

The present paper characterises the photometric system defined by the WFCAM $ZYJHK$ broadband filters. The layout of the of the paper is as follows. In Section 2 we explain the design of the five passbands, in Section 3 we explain the procedure for computing synthetic colours, and in Section 4 assemble the required ingredients. In Section 5 we present the synthetic colours of a variety of non–degenerate and degenerate stars, galaxies, and quasars. Finally, in Section 6 we compute colour equations between certain WFCAM, SDSS, and 2MASS filters. A future paper (Hodgkin et al., 2006) will describe the results of calibration observations with the instrument, and present the measured colour terms. These two papers, then, are similar in aim to the SDSS papers by Fukugita et al. (1996) and Smith et al. (2002).

2 THE WFCAM $ZYJHK$ PHOTOMETRIC SYSTEM

Extensive work on the specification of optimal passbands in the near-infrared has led to the development of the Mauna Kea Observatories (MKO) near-infrared filter set that includes $JHKL'M'$ bandpasses (Simons & Tokunaga 2002; Tokunaga, Simons & Vacca 2002). The MKO filters have been adopted widely and the filters chosen for the WFCAM J, H and K bands have been manufactured to the MKO specifications.

Key science goals of UKIDSS include a census of very low temperature brown dwarfs (Section 5.2.2) and the identification of quasars with redshifts beyond the current maximum reached by SDSS, $z = 6.4$ (Section 5.4). To enable such goals, a novel feature of UKIDSS is the extension of imaging observations to wavelengths shortward of $1.2\,\mu$m where the availability of broadband colours improves the discrimination between brown dwarfs and high-redshift quasars.

At the interface between conventional optical and near-infrared observations the SDSS z-band has in practice become the "standard" and the availability of extensive sky-coverage in the z-band from the SDSS is an important element for the exploitation of the UKIDSS LAS. There is thus an argument for incorporating the SDSS z-band, or a very close approximation to the band, into the UKIDSS filter set. However, while the SDSS z-band is well-defined, a feature of the passband is an extended tail in the response curve extending to long wavelengths. The SEDs of low-mass stars, brown dwarfs and high-redshift quasars involve both steeply rising flux distributions towards red wavelengths, coupled with large spectral discontinuities. As a result, the magnitude difference between the SDSS z-band and a passband with a more rectangular or Gaussian transmission profile can be large for red objects. Furthermore, the form of the extended red tail in the SDSS z-band is defined by the declining CCD detector quantum efficiency and is also affected by strong atmospheric absorption at $0.93 - 0.97\,\mu$m, making the synthesis of a passband closely similar to the SDSS z-band impractical. For these reasons a new Z-band filter has been designed for use with WFCAM. The specification involves: an effective wavelength of $0.882\,\mu$m (close to the effective wavelength of the SDSS z-band), close to constant transmission over a $0.06\,\mu$m wavelength range, and cut–on and cut–off profiles very similar to the MKO JHK filters.

The wavelength interval between $0.9\,\mu$m and $1.2\,\mu$m has, until now, been largely unexploited. The low sensitivity of most optical CCD detectors at $\sim 1\,\mu$m, coupled with the relatively bright sky-background curtailed interest from optical astronomers. For infrared astronomers, the lack of large near-infrared detectors, that would enable wide-field surveys to be undertaken, has meant that observations at $\sim 1\,\mu$m would be of interest in only a few specialised applications. For the first time, the technological advance represented by the commissioning of WFCAM allows wide-field observations with an instrument that possesses high throughput at $\sim 1\,\mu$m. Scientifically, the aim of detecting bright quasars with redshifts as high as $z = 7.2$, provides a strong motivation for obtaining broadband observations at wavelengths between the Z and J bands.

To this end, Warren & Hewett (2002) proposed a specification for a new Y-band filter with an effective wavelength of $1.03\,\mu$m. Hillenbrand et al. (2002) have also defined and characterised a Y-band filter with a similar effective wavelength but a substantially greater width. The rationale for the choice of the narrower Y band involves avoiding the wavelength region that suffers from significant atmospheric absorption by adopting a blue cut-on wavelength of $\simeq 0.97\,\mu$m. At the red end of the passband, the onset of very strong emission from OH lines occurs at $1.07\,\mu$m. This increases the signal from the sky background significantly and the Warren & Hewett Y-band cut–off wavelength is chosen to be $\simeq 1.07\,\mu$m in order to reduce the effect of the sky background. The narrower passband also has the significant advantage of allowing improved discrimination between high-redshift quasars and T dwarfs, by some 0.15 mag. The narrower Y-band specification has therefore been adopted for the UKIDSS Y-band filter and several other observatories have also decided to incorporate the narrower Y-band

specification in their filter sets (A. Tokunaga, private communication).

3 SYNTHETIC PHOTOMETRY

All calculations of magnitudes and colours have been undertaken using the **synphot** package in the Space Telescope Science Data Analysis System. The mean flux density, $f_\lambda(P)$, in a broad passband defined by a dimensionless bandpass throughput function, $P(\lambda)$, is calculated as:

$$f_\lambda(P) = \frac{\int P(\lambda) f_\lambda(\lambda) \lambda d\lambda}{\int P(\lambda) \lambda d\lambda} \quad (1)$$

where $f_\lambda(\lambda)$ is the flux density of the target object (Synphot User Guide 1998[2]). The associated zero-point is calculated by evaluating the same expression for a spectrophotometric standard star, Vega in our case, "observed" using the identical passband function $P(\lambda)$. The technique is thus differential in nature and mimics the procedure undertaken when performing actual photometric observations, calibrated by observations of standard stars. The shape of the throughput function is the key element in the calculation, although, for all but the most pathological of target SEDs, errors in the form of the throughput function cancel to first-order because the zero-point defined by the standard star is calculated using the same throughput function.

Synphot employs a reference SED for Vega from Bohlin & Gilliland (2004). Since in the system of the UKIRT Faint Standards (Hawarden et al., 2001), that will be used to calibrate UKIDSS, Vega has zero magnitude in J, H, and K, whereas in the Johnson UBV system Vega has non–zero magnitudes, care must be taken in defining zero-points. *In this paper the zero-points in all the UKIDSS, SDSS, and 2MASS bands are defined by Vega having zero magnitude.* Transfer to a system in which Vega has non-zero magnitude (as is the case for some near–infrared systems) can be achieved by a simple zero-point shift. Offsets to the AB system are provided in section 4.6.

3.1 Accuracy of zero points

We assume that the spectrum of Vega provided by Bohlin & Gilliland (2004) is an accurate representation of the true SED. Employing this spectrum as the basis for the calculations presented here ensures that the results are reproducible by others. If an improved determination of the Vega spectrum becomes available it would therefore be a simple matter to compute adjustments to any quantities provided here.

Extensive work has been undertaken to determine the absolute flux-distribution of Vega from the ultraviolet through near-infrared wavelengths (e.g. Bohlin & Gilliland (2004); Cohen, Wheaton, & Megeath (2003)) but uncertainty at the 2% level remains (see Tokunaga & Vacca (2005) for a recent discussion). A particular concern is whether the near-infrared absolute fluxes of Vega should be increased by $\simeq 2\%$ relative to those in the optical. While the basis for the calculation of the magnitudes and colours presented here is clear, i.e. the Bohlin & Gilliland Vega spectrum has zero magnitude for all passbands, if systematic offsets in magnitude or colour at the few per cent level are an issue for a particular application, careful reference should be made to the above emphasised statements on the zero-points definition, and the adopted SED.

[2] `http://www.stsci.edu/resources/software_hardware/stsdas/synphot`

Table 1. Wavelength dependence of array detector q.e.

λ μm	0.8	0.9	1.0	1.1	1.2	1.4	1.6	2.2
q.e.	0.55	0.57	0.57	0.56	0.56	0.59	0.64	0.63

4 RESPONSE FUNCTIONS

Passband response functions have been computed by taken into consideration all wavelength–dependent quantities, including atmospheric absorption, mirror reflectivity, filter transmission, and array quantum efficiency. Wavelength–independent quantities are irrelevant for synthesising colours, but have been included by normalising the computed curves to the measured total system throughput established from observations of standard stars. This result is preliminary, and the overall wavelength–independent normalisation applied is subject to revision.

4.1 Atmospheric Transmission

The effect of atmospheric transmission was quantified using the ATRAN code (Lord 1992). Models were generated over the wavelength range $0.8 - 2.5\,\mu$m with a resolution of 3 Å using atmospheric parameters appropriate for observations from Mauna Kea. Using four values for the airmass (1.0, 1.3, 1.6 and 2.0) and four values for the precipitable water-vapour (1.0, 2.0, 3.0 and 5.0 mm) resulted in a total of 16 models. The vast majority of the UKIDSS observations are expected to be performed at airmass $\leqslant 1.3$ with a water-column of $\simeq 1.0$ mm. However, more extreme airmass values and water-columns up to 5 mm were included to allow investigation of the passband behaviour in both poor conditions on Mauna Kea and for sites with much larger values of precipitable water-vapour, such as those employed for 2MASS. The impact of Rayleigh scattering and aerosol scattering (Hayes & Latham 1975) on the shape of the passbands is insignificant given our target photometric accuracy and no attempt has been made to include their effects.

4.2 Telescope, Instrument and Detector

Light entering the telescope undergoes three reflections from aluminium-coated mirrors (telescope primary, telescope secondary and one reflection within WFCAM) before reaching the detectors. The variation in reflectivity at short infrared wavelengths, relevant for the Z and Y bands, is significant and three reflections from aluminium have been incorporated in the calculation of the passbands using data from Hass & Hadley (1963).

Transmission measurements over the wavelength range of interest for the remaining optical components within

Table 2. System throughput curve for the WFCAM Z filter

λ μm	throughput
0.803	0.000
0.804	0.001
0.805	0.001
0.806	0.001
0.807	0.001

Note: The full table is published in the electronic version of the paper. A portion is shown here for guidance regarding its form and content.

Table 3. System throughput curve for the WFCAM Y filter

λ μm	throughput
0.952	0.000
0.953	0.001
0.954	0.001
0.955	0.001
0.956	0.001

Note: The full table is published in the electronic version of the paper. A portion is shown here for guidance regarding its form and content.

the WFCAM instrument show no variations exceeding 1%, and constant transmission, independent of wavelength, has therefore been adopted.

The quantum efficiency of the Rockwell Hawaii-II 2048×2048 HgCdTe detectors increases approximately linearly with wavelength. The change across the individual passbands amounts to only a few per cent but the variation in quantum efficiency has been incorporated in the calculation of the passbands using data for a typical device (Table 1). The measurements at 1.2, 1.6, and 2.2μm are the values supplied by the manufacturer. To obtain the remaining values in the table, the relative quantum efficiency across the interesting wavelength range was measured by the WFCAM team (Casali et al, 2006), and the values were normalised to the manufacturer's points. We have interpolated between the points in the table, with the quantum efficiency assumed to be constant for wavelengths $> 2.2\,\mu$m.

4.3 Filters

The filter transmission curves are from laboratory measurements at 10 Å intervals, made by the WFCAM team. The measurements were undertaken at room temperature. The dependence of the filter cut-on and cut-off wavelengths as a function of temperature was measured by the manufacturers. Filter transmission curves appropriate for the operating temperature (120 K) of the WFCAM instrument were then derived by us by applying the measured temperature dependence at the cut–on and cut–off wavelengths, with linear interpolation adopted for wavelengths between the two reference points. For the Z filter the measured temperature dependence was consistent with no change and the transmission profile measured at room temperature was used. At the other extreme, the K-filter exhibits a shift of $\simeq 0.035\,\mu$m, or $\sim 10\%$ of the bandwidth, and the use of the temperature–corrected profiles is important when calculating passbands.

Table 4. System throughput curve for the WFCAM J filter

λ μm	throughput
1.130	0.000
1.131	0.001
1.132	0.001
1.133	0.001
1.134	0.001

Note: The full table is published in the electronic version of the paper. A portion is shown here for guidance regarding its form and content.

Table 5. System throughput curve for the WFCAM H filter

λ μm	throughput
1.421	0.000
1.422	0.001
1.423	0.000
1.424	0.000
1.425	0.001

Note: The full table is published in the electronic version of the paper. A portion is shown here for guidance regarding its form and content.

Table 6. System throughput curve for the WFCAM K filter

λ μm	throughput
1.917	0.000
1.918	0.001
1.919	0.001
1.920	0.000
1.921	0.000

Note: The full table is published in the electronic version of the paper. A portion is shown here for guidance regarding its form and content.

The transmission measurements were undertaken from $0.4\,\mu$m out to beyond $3.0\,\mu$m, where the WFCAM detectors possess no sensitivity. With the exception of an insignificant narrow "blue leak" of height 1% at $\simeq 0.792\,\mu$m for the Y filter, no leaks above the 0.1% specification requirement were present in any of the filter transmission curves.

The transmission curves presented here are derived from a single filter in each band — four filters per band are necessary to cover the detector arrays in WFCAM — but intercomparison of the four transmission curves in each band shows that the variations between filters produce differences in the photometry of at most 0.01 magnitudes.

4.4 Summary: WFCAM system throughput curves

Fig. 1 shows the $ZYJHK$ passband transmission curves for: i) no atmosphere, ii) typical atmospheric conditions, airmass 1.3 and 1.0 mm of precipitable water-vapour, and iii) extreme atmospheric conditions, airmass 2.0 and 5.0 mm of precipitable water-vapour.

The MKO JHK filter transmissions were developed with the aim of minimising the effects of variable atmospheric transmission due primarily to the change in the water content of the atmosphere. The same philosophy was adopted in the design of the new Z and Y filters. The result is a reassuring stability of the UKIDSS $ZYJHK$ system over a wide range of atmospheric conditions. There are essentially

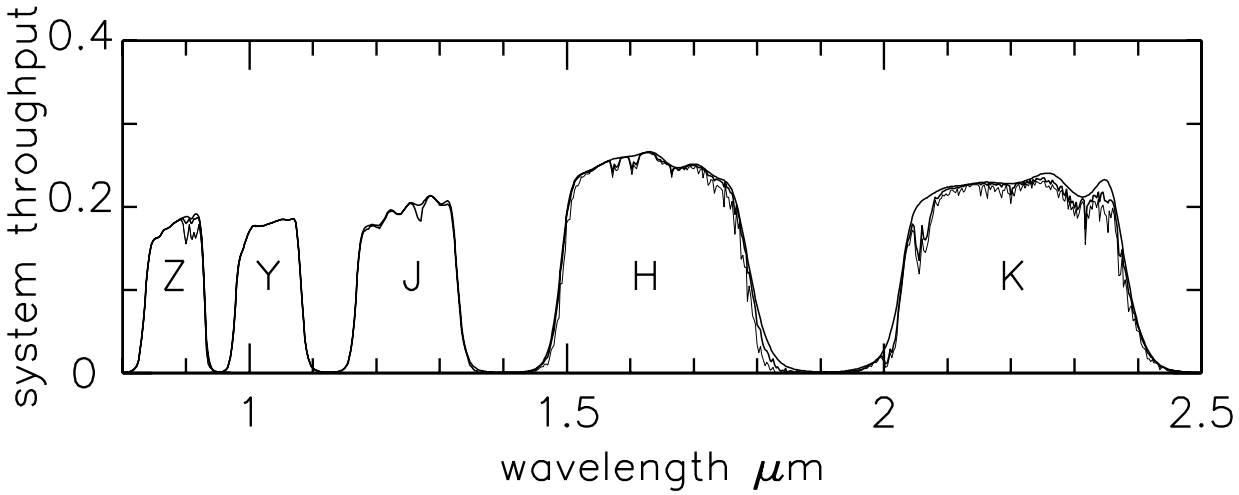

Figure 1. Transmission curves, from above atmosphere to detector, for the WFCAM filter set. Three curves are shown for each band. The upper, thick, curve is for no atmospheric absorption. The middle, thick, curve is for the default atmospheric conditions (1.3 airmass, 1.0mm water), and the lower, thin, curve is for extreme atmospheric conditions (2.0 airmass, 5.0 mm water). These curves have been computed on the basis of measurement or modelling of the relevant wavelength–dependent quantities. An overall wavelength–independent normalisation has been applied to match the photon count rate measured for standard stars with the instrument. The calculation is preliminary and the wavelength–independent normalisation is subject to revision.

no differences in the photometry at the > 0.01 mag level for objects with non-pathological SEDs for observations made through precipitable water-vapour columns of $\leqslant 3.0$ mm and at airmasses in the range $1.0 - 1.6$.

Consider observations of the full range of stellar types included in the Bruzual–Persson–Gunn–Stryker atlas (Section 5.1.1). Even for observations made at an airmass of 2.0 through an extreme atmospheric model for Mauna Kea that includes 5.0 mm of water-vapour (Fig. 1), only in the Z-band, for a narrow range of stellar type (M6-M8), are differences in the photometry that exceed > 0.01 mag level evident. The differences in the Z-band, compared to observations made in excellent conditions, amount to no more than 0.015 mag for the narrow range of late-M spectral types. Similarly, for the adopted quasar SED (Section 5.4), differences between observations made through the extrema of the atmospheric models differ by less than 0.02 mag for redshifts $z < 6.2$. Only at redshifts ($z \sim 6.5$) where the very strong spectral discontinuity at Lyman-α 1216 Å coincides with the atmospheric absorption at $9000 - 9200$ Å in the Z-band does the photometry differ by more than 0.1 mag, reaching a maximum of 0.2 mag.

Synthetic photometry for such truly unusual SEDs observed through the most extreme atmospheric models can be obtained using the appropriate transmission curves. However, for the calculations presented in this paper we have adopted the passband transmission curves based on observations at an airmass of 1.3 through an atmosphere with 1.0 mm of precipitable water-vapour, typical of the conditions under which the majority of UKIDSS data are likely to be obtained. These default $ZYJHK$ passband transmissions are provided in Tables 2–6.

Table 7. Conversion to AB mag.

band	$\lambda_{\rm eff}$ μm	S Jy	flux density W m$^{-2}\mu^{-1}$	AB offset
u	0.3546	1545	3.66×10^{-8}	0.927
g	0.4670	3991	5.41×10^{-8}	-0.103
r	0.6156	3174	2.50×10^{-8}	0.146
i	0.7471	2593	1.39×10^{-8}	0.366
z	0.8918	2222	8.32×10^{-9}	0.533
Z	0.8817	2232	8.59×10^{-9}	0.528
Y	1.0305	2026	5.71×10^{-9}	0.634
J	1.2483	1530	2.94×10^{-9}	0.938
H	1.6313	1019	1.14×10^{-9}	1.379
K	2.2010	631	3.89×10^{-10}	1.900

4.5 SDSS and 2MASS Passbands

The SDSS passbands are based on data obtained by J. Gunn to calculate the "June 2001" version of the SDSS passbands, which were kindly supplied by X. Fan. The passbands are appropriate for the observation of point sources from Apache Point Observatory at an airmass of 1.3.

The 2MASS passbands were derived by taking the relative spectral response curves given by Cohen et al. (2003), dividing by wavelength and renormalising to produce a transmission function, $P(\lambda)$, as employed in equation 1.

4.6 AB system offsets

In Table 7 we list the filters and provide in col. 2 the computed effective wavelength, defined according to Schneider, Gunn & Hoessel (1983) (see equation 3 in Fukugita et al. 1996). Cols 3 and 4 list the flux-density of an object spectrum, of constant flux density in both Jy and $\mathrm{Wm}^{-2}\mu^{-1}$, over each passband, that corresponds to zero magnitude. The former quantity is quantified in another way in col. 5, as the magnitude offset to convert the Vega-based magnitudes onto the AB-magnitude system (Oke and Gunn, 1983), where we have used the definition $AB_\nu = -2.5 \log f_\nu \, (\mathrm{erg\,s^{-1}cm^{-2}Hz^{-1}}) + 48.60$. The values for the J, H, and K bands computed by Tokunaga and Vacca (2005), for the MKO system, are virtually identical. This is a coincidence, however, as they employed a slightly different SED for Vega, and a different zero–point of the AB system, these two differences closely cancelling each other.

5 SYNTHETIC COLOURS OF STARS, GALAXIES, AND QUASARS

In this section we use the apparatus described in Sections 3 and 4, to synthesise colours of a wide range of sources — stars, galaxies, and quasars — to illustrate the colours of the types of objects expected to appear in the surveys. The following sub–sections detail the origins of the spectra, and tabulate the results for each class of object. Fig. 2 (for brown dwarfs, stars and quasars) and Fig. 3 (for galaxies) illustrate the Z, Y, J, H, K, colours which are discussed in the relevant sub-sections that follow. Because of the wide range of computed colours, in each of the two figures the left–hand set of panels and the right-hand set of panels show the same two–colour diagrams at different scales. As discussed in Section 4.4 all calculations presented employ the passband transmission functions appropriate to observations at airmass 1.3 through an atmosphere with 1.0 mm of precipitable water-vapour.

The results shown here may be reproduced by taking the tabulated passband transmissions, $P(\lambda)$ (Tables 2−6), and evaluating the quantity $f_\lambda(P)$ defined in equation 1, for a particular object SED (provided in the form $f_\lambda(\lambda)$). The zero-point is derived by performing the same calculation for the Bohlin & Gilliland (2004) Vega spectrum. Colours in the same system may be computed for any object of specified SED by following this procedure.

5.1 Non-degenerate stars: the BPGS spectrophotometric atlas, and additional M dwarfs

5.1.1 BPGS spectrophotometric atlas

The Bruzual–Persson–Gunn–Stryker (BPGS) atlas is a database of spectrophotometry of 175 stars, of a wide range of spectral type and luminosity class, spanning the optical and near–ir wavelength range. The atlas itself is unpublished, but is available at e.g. `http://www.stsci.edu/hst/observatory/cdbs/bpgs.html`. The optical spectra comprise the Gunn–Stryker atlas (Gunn & Stryker, 1983). Most of the near-infrared data come from Strecker, Erickson & Witteborn (1979), while the remainder are unpublished. Stars 1–12, 70–77, 173, and 174 have been omitted from the calculations due to incomplete wavelength coverage. Stars 169, and 170 were also excluded because of an apparent mismatch between the amplitudes of the optical and near-infrared spectra.

The synthesised colours of the BPGS stars are provided in Table 8. The first 12 columns list colours from u to K, and columns $13-15$ list successively the spectral classification, the BPGS reference number and the name of the star, taken from Gunn & Stryker (1983), if provided.

5.1.2 Additional M dwarfs

The BPGS atlas contains spectra of only six M dwarfs. Therefore we have supplemented the list with spectra of 15 M dwarfs covering the wavelength range i to K, collated from the following references: Geballe et al. (2002), Hawley, Gizis & Reid (1996), Henry, Kirkpatrick & Simons (1996), Kirkpatrick, Henry & Simons (1995), Leggett et al. (2000a; 2001; 2002a), McLean et al. (2003), and Reid, Hawley & Gizis (1995). In Table 9, cols $1-9$ provide colours over the range i to K, col. 10 gives the K-band absolute magnitude, M_K, with the source of the parallax determination indicated, col. 11 provides the spectral classification and col. 12 the object name. In a few cases the spectrum does not cover the entire i band, and the $i-z$ entry is consequently blank. The spectra were observed in a small number (e.g. three) of sections, each spectrophotometrically calibrated. To account for differential slit losses, the sections of spectra were calibrated absolutely using published photometry, in J, H, and K, and frequently in a wide Z filter that covers the entire range of the WFCAM Z and Y filters. The result is that our synthesised colours to a large extent simply reproduce the published colours in the J, H, and K bands, whereas colours that include the i, Z, and Y bands involve a degree of interpolation or extrapolation, and therefore will be less accurate. The uncertainties in the spectral fluxes (at wavelengths within the WFCAM photometric passbands) are typically 3%. Deviations between the measured JHK colours and the slopes of the spectra are 1-5%. Hence the errors in the predicted colours of the M-dwarfs, and the L and T dwarfs discussed in Section 5.2.1, are expected to be 0.03-0.06 mag.

In Fig. 2 the colours of BPGS dwarfs covering the range of spectral types from O to K, are plotted as blue filled circles. M dwarfs are plotted as green open circles, and extend the colour sequence displayed by the O to K dwarfs to redder colours.

5.2 Degenerate stars: L and T dwarfs, model Y dwarfs, and cool white dwarfs

5.2.1 L and T dwarfs

Colours of 30 L dwarfs and 22 T dwarfs have been computed from spectra covering the wavelength range i to K, collated from the following references: Burgasser et al. (2003), Chiu et al. (2006, submitted), Cruz et al. (2003), Fan et al. (2000a), Geballe et al. (1996), Geballe et al. (2001), Geballe et al (2002), Kirkpatrick, Beichman & Skrutskie (1997), Kirkpatrick et al. (1999b), Kirkpatrick et al. (2000), Knapp et al. (2004), Leggett et al (2000; 2001; 2002a; 2002b),

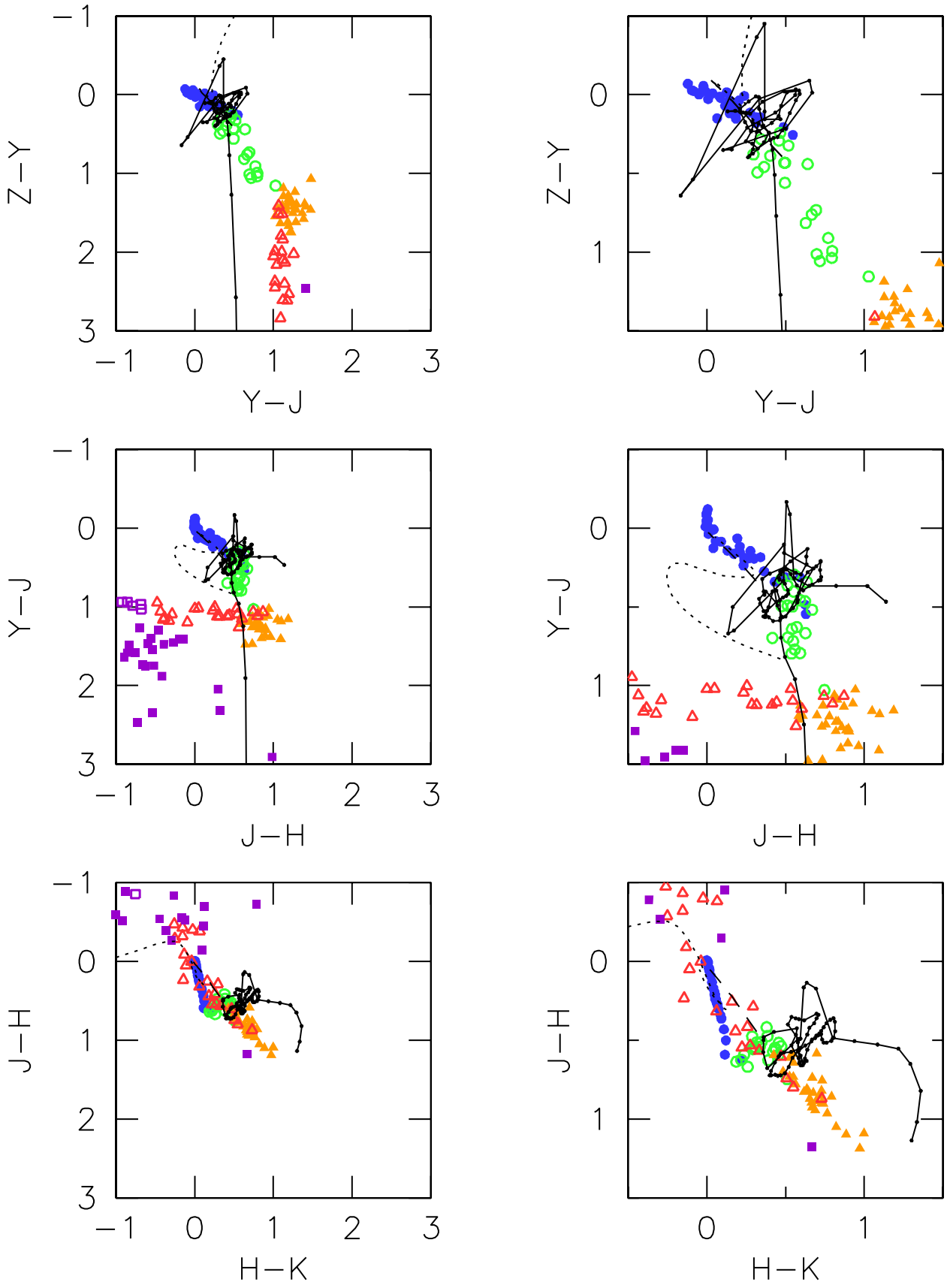

Figure 2. Top to bottom, three 2–colour diagrams of stellar sources, cycling through the colour sequence $Z-Y$, $Y-J$, $J-H$, $H-K$. Each right–hand panel is a 2× expanded view of part of the corresponding left–hand panel. Key: BPGS O–K dwarfs blue ●; M dwarfs green ◯; L dwarfs orange ▲; T dwarfs red △; Burrows model cool brown dwarfs purple ■; Marley model cool brown dwarfs purple □; quasars $0 < z < 8.5$, $\Delta z = 0.1$, solid black line; H white dwarfs dotted black line, He white dwarfs dashed black line.

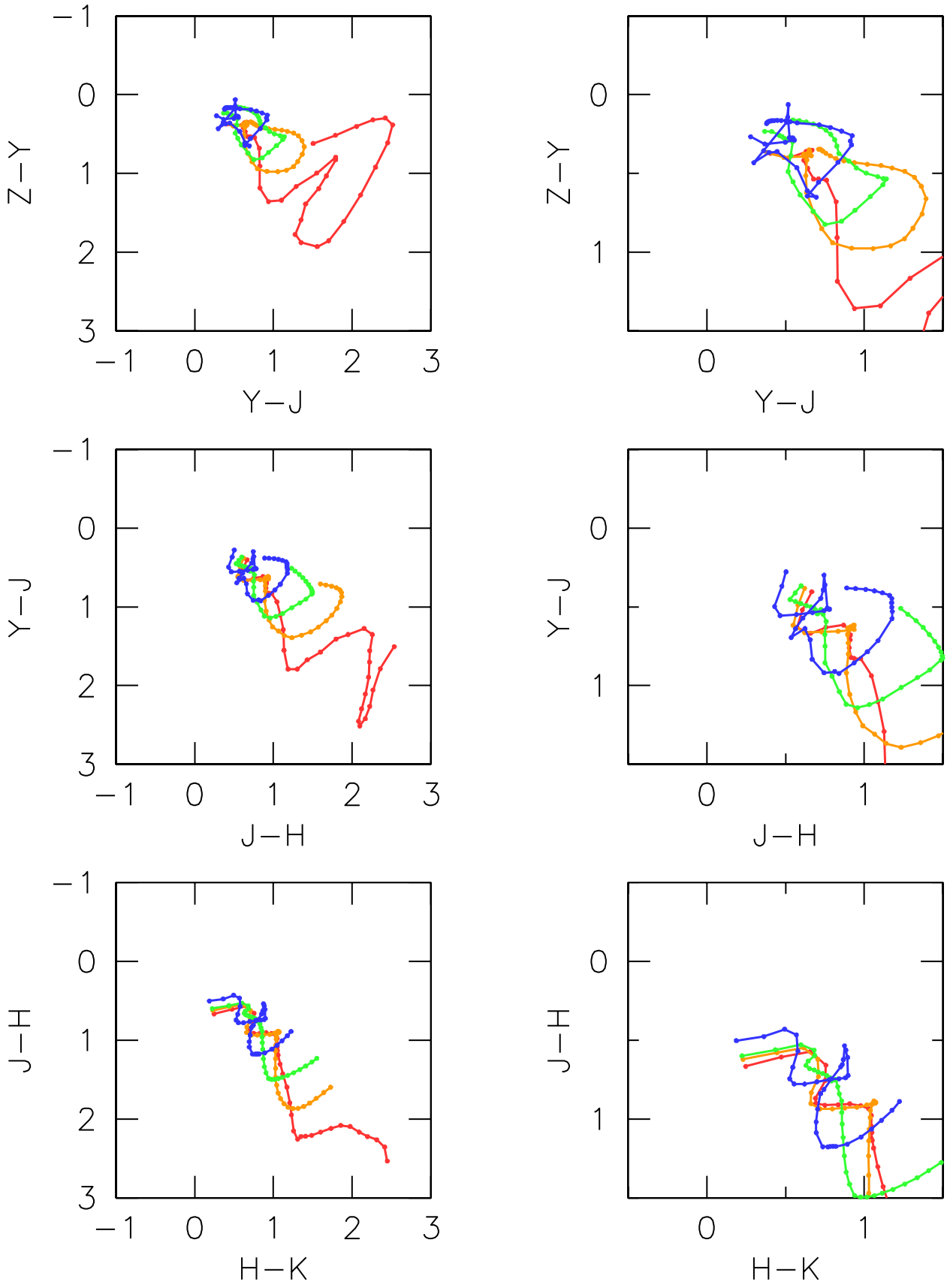

Figure 3. Top to bottom, three 2–colour diagrams of *hypeprz* galaxy templates, redshift range $0 < z < 3.6$, $\Delta z = 0.1$, cycling through the colour sequence $Z-Y$, $Y-J$, $J-H$, $H-K$. Each right–hand panel is a 2× expanded view of part of the corresponding left–hand panel. Key: E red, Sbc orange, Scd green, Im blue.

Table 8. Colours of selected stars from the BPGS atlas

u–g	*g–r*	*r–i*	*i–z*	*Z–z*	*Z–Y*	*Y–J*	*J–H*	*H–K*	*J–J2*	*H–H2*	*K–K2*	Class	BPGS no.	Name
-0.456	-0.066	-0.029	0.031	-0.012	-0.069	-0.120	0.006	-0.002	0.007	0.000	-0.001	B9V	13	HD189689
-0.043	-0.010	0.011	0.034	-0.010	-0.027	-0.094	0.000	-0.008	0.009	0.002	-0.002	A0V	14	THETA-VIR
-0.133	-0.019	0.027	0.040	-0.002	-0.023	-0.084	-0.003	-0.007	0.009	0.001	-0.002	B9V	15	NU-CAP
-0.012	-0.002	0.005	0.000	-0.008	-0.056	-0.021	0.003	-0.007	0.003	0.001	-0.002	A2V	16	HR6169
-0.068	-0.002	0.017	0.036	-0.002	-0.022	-0.010	-0.008	0.001	0.006	0.001	-0.002	A1V	17	HD190849A

Note: The full table is published in the electronic version of the paper. A portion is shown here for guidance regarding its form and content.

Table 9. Colours of selected additional M dwarfs

i–z	*Z–z*	*Z–Y*	*Y–J*	*J–H*	*H–K*	*J–J2*	*H–H2*	*K–K2*	M_K	Class	Name
0.576	0.021	0.323	0.519	0.668	0.260	-0.034	0.020	-0.008	5.3[a]	M1	Gl 229A
...	-0.014	0.292	0.458	0.593	0.237	-0.040	0.020	-0.038	8.2[b]	M3	LHS 5327
0.973	0.032	0.432	0.498	0.543	0.303	-0.037	0.026	-0.019	7.8[b]	M3.5	GJ 1001A
0.966	0.017	0.440	0.640	0.541	0.337	-0.053	0.026	-0.025	8.1[a]	M3.5	Gl 15B
1.147	0.023	0.432	0.492	0.514	0.316	-0.044	0.021	-0.052	8.2[a]	M4	Gl 699
0.957	0.055	0.559	0.496	0.476	0.288	-0.040	0.028	-0.029	6.9[b]	M4.5	Gl 630.1A
0.858	0.078	0.815	0.628	0.571	0.421	-0.040	0.027	-0.032	9.0[b]	M5.5	GJ 1002
1.508	0.113	1.056	0.718	0.548	0.433	-0.049	0.034	-0.031	9.5[b]	M5.5	GJ 4073
1.337	0.077	0.733	0.694	0.516	0.457	-0.048	0.031	-0.035	8.5[b]	M5.5	GJ 1245A
1.170	0.060	0.761	0.667	0.627	0.391	-0.052	0.025	-0.024	8.4[b]	M5.5	Gl 905
1.550	0.089	0.909	0.771	0.559	0.439	-0.050	0.029	-0.024	9.1[b]	M6	Gl 406
...	0.037	1.012	0.698	0.417	0.380	-0.064	0.029	-0.053	8.7[b]	M6	LHS 5328
1.720	0.120	1.036	0.794	0.593	0.455	-0.055	0.034	-0.025	9.7[b]	M6.5	GJ 3855
1.559	0.092	0.992	0.796	0.538	0.472	-0.065	0.037	-0.026	9.7[b]	M7	VB 8
2.299	0.157	1.154	1.028	0.747	0.511	-0.051	0.034	-0.016	...	M8.5	SDSS J225529.09-003433.4

a ESA (1997)
b van Altena, Lee & Hoffleit (1995)

Liebert et al. (2000), McLean et al. (2003), Reid et al. (2001), Schultz et al. (1998), Strauss et al. (1999), Tinney et al. (1998), and Tsvetanov et al. (2000). In Table 10, cols $1-9$ provide colours over the range i to K, col. 10 gives the K-band absolute magnitude, M_K, with the source of the parallax determination indicated, col 11. provides the spectral classification and col. 12 lists the object name. As with the M dwarfs, in a few cases the spectrum does not cover the entire i band, and the $i-z$ entry is consequently blank. The accuracy of the synthetic colours that include the i, Z, Y bands is subject to the same remarks made above in relation to the M dwarfs.

The colours of very cool stars, of spectral type M, L, and T, across the WFCAM bands, deserve comment. In the $J-H$ *vs* $H-K$ two-colour diagram, Fig. 2, moving down the brown dwarf sequence, the early L stars firstly extend the O to M colour sequence to redder colours. Moving to cooler temperatures the colours reverse and track back up the colour sequence, becoming successively bluer, until the coolest T dwarfs are bluer than O stars (due to the presence of strong absorption bands of water, methane and pressure-induced H_2; see e.g. Burgasser et al. 2002; Geballe et al. 2002). The consequence is that over a broad temperature range, from mid L to mid T, the $J-H$ *vs* $H-K$ two–colour diagram is ineffective for distinguishing brown dwarfs from hydrogen burning stars. A two-colour diagram involving Z, such as $Z-J$ *vs* $J-H$ separates the two populations. Nevertheless very deep observations would be required in Z to detect the coolest T dwarfs, which have $Z-J\sim 4$. The Y band provides a compromise solution. In the $Y-J$ *vs* $J-H$ diagram, plotted in the middle panels in Fig. 2, it is seen that brown dwarfs have approximately constant $Y-J\sim 1.2$, redder than the M stars, while the $J-H$ colour (or $J-K$) separates the L dwarfs from the T dwarfs.

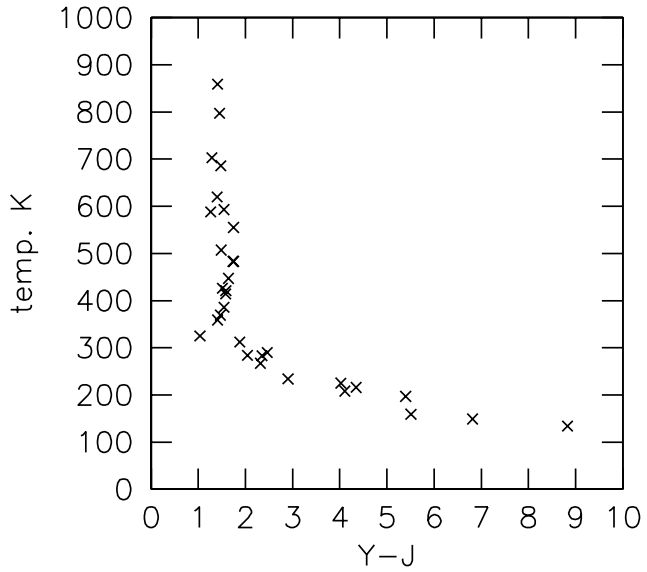

Figure 4. Temperature–colour relation of model cool brown dwarfs

5.2.2 Model Y dwarfs

The current coolest known T dwarf is 2MASSJ0415-0935 (Burgasser et al. 2002). The synthetic colours for this ob-

Table 10. Colours of selected L and T dwarfs

i−*z*	*Z*−*z*	*Z*−*Y*	*Y*−*J*	*J*−*H*	*H*−*K*	*J*−*J*2	*H*−*H*2	*K*−*K*2	Class	Name
2.077	0.100	1.069	1.476	0.643	0.549	-0.085	0.041	-0.016	L1	2MASS J03454316+2540233
1.996	0.188	1.322	1.193	0.610	0.527	-0.073	0.045	0.007	L1	2MASS J07464256+2000321AB
2.165	0.232	1.419	1.412	1.092	0.997	-0.096	0.058	-0.020	L3	2MASS J00283943+1501418
...	0.251	1.460	1.289	0.819	0.729	-0.094	0.056	-0.024	L3	SDSS dummy
2.064	0.187	1.385	1.397	0.850	0.718	-0.088	0.055	-0.020	L3	DENIS-P J1058.7-1548
2.137	0.248	1.503	1.366	0.896	0.665	-0.085	0.048	-0.011	L3	GD 165B
2.138	0.215	1.458	1.472	0.733	0.550	-0.100	0.055	-0.004	L4	2MASS J00361617+1821104
...	0.168	1.235	1.274	0.899	0.728	-0.102	0.057	-0.017	L4.5	SDSS dummy
2.337	0.254	1.418	1.263	0.857	0.792	-0.093	0.056	-0.015	L4.5	LHS 102 B
2.139	0.231	1.392	1.291	0.902	0.738	-0.096	0.058	-0.017	L4.5	SDSS dummy
2.719	0.214	1.359	1.230	0.821	0.643	-0.096	0.054	-0.013	L5	SDSS dummy
2.789	0.196	1.443	1.062	0.810	0.636	-0.102	0.056	0.004	L5.5	DENIS-P J0205.4-1159AB
...	0.317	1.577	1.383	0.963	0.764	-0.101	0.056	-0.017	L5.5	SDSS dummy
2.884	0.181	1.411	1.158	1.186	0.971	-0.105	0.057	-0.029	L5.5	SDSS dummy
1.472	0.194	1.375	1.195	0.778	0.563	-0.111	0.052	-0.009	L5.5	SDSS dummy
2.949	0.196	1.616	1.182	1.097	0.884	-0.094	0.056	-0.024	L6	2MASS J08251968+2115521
...	0.230	1.419	1.261	0.730	0.525	-0.107	0.052	-0.011	L6	SDSS dummy
...	0.188	1.286	1.126	0.738	0.669	-0.105	0.062	-0.011	L6	SDSS dummy
2.494	0.257	1.615	1.284	0.885	0.695	-0.103	0.057	-0.011	L6	DENIS-P J1228.2-1547AB
1.317	0.298	1.501	1.246	0.756	0.732	-0.086	0.048	-0.028	L6	SDSS dummy
...	0.390	1.747	1.229	0.834	0.675	-0.107	0.054	-0.013	L6.5	SDSS dummy
...	0.202	1.280	1.188	0.699	0.484	-0.100	0.053	-0.013	L6.5	SDSS dummy 221557.1
3.105	0.168	1.461	1.160	1.049	0.822	-0.108	0.056	-0.009	L7.5	2MASS J16322911+1904407
...	0.173	1.184	1.125	0.594	0.425	-0.113	0.058	-0.021	L7.5	SDSS dummy
...	0.176	1.406	1.112	0.928	0.667	-0.112	0.057	0.004	L8	SDSS dummy
...	0.247	1.631	1.089	0.827	0.618	-0.124	0.060	-0.004	L9	SDSS dummy
3.089	0.198	1.470	1.133	0.870	0.653	-0.107	0.055	-0.013	L9	2MASS J09083803+5032088
3.201	0.197	1.542	1.025	0.942	0.688	-0.117	0.060	0.034	L9	2MASS J03105986+1648155
1.765	0.354	1.738	1.215	0.587	0.546	-0.112	0.052	-0.008	L9.5	SDSS dummy
...	0.272	1.664	1.193	0.583	0.698	-0.143	0.050	-0.001	L9.5	SDSS dummy
2.605	0.184	1.513	1.066	0.870	0.730	-0.135	0.062	-0.004	T0	SDSS dummy
3.044	0.220	1.517	1.114	0.799	0.550	-0.125	0.058	-0.003	T0	SDSS dummy
...	0.148	1.410	1.066	0.743	0.506	-0.140	0.058	0.001	T0	SDSS dummy
1.527	0.422	2.133	1.148	0.604	0.472	-0.153	0.057	0.023	T1	SDSS dummy
1.903	0.276	1.787	1.097	0.546	0.224	-0.147	0.059	0.045	T1.5	SDSS dummy
3.684	0.310	2.020	1.257	0.567	0.332	-0.179	0.067	0.041	T2	SDSS dummy
4.712	0.325	1.989	1.021	0.534	0.275	-0.168	0.063	0.054	T2	SDSS dummy
1.550	0.223	1.835	1.121	0.414	0.258	-0.170	0.053	0.058	T2.5	SDSS dummy
...	0.280	2.048	1.004	0.255	0.160	-0.151	0.056	0.064	T3	2MASS J12095613-1004008
...	0.313	2.100	1.119	0.287	0.295	-0.193	0.062	0.046	T3	SDSS dummy
3.352	0.296	1.991	1.105	0.443	0.183	-0.187	0.057	0.056	T3	SDSS dummy
...	0.390	2.157	1.044	0.234	-0.144	-0.179	0.045	0.076	T3	SDSS dummy
1.976	0.509	2.608	1.122	0.317	0.062	-0.212	0.070	0.090	T3.5	SDSS dummy
...	0.487	2.447	1.020	0.050	-0.108	-0.188	0.049	0.107	T4	2MASS J22541892+3123498
4.590	0.491	2.526	1.198	-0.090	-0.131	-0.211	0.046	0.119	T4.5	2MASS J05591914-1404488
3.357	0.423	2.372	1.021	0.001	-0.038	-0.203	0.048	0.104	T4.5	SDSS dummy
...	0.612	2.836	1.091	-0.288	-0.251	-0.222	0.041	0.110	T4.5	SDSS dummy
4.009	0.477	2.614	1.178	-0.321	-0.152	-0.258	0.038	0.131	T6	SDSS dummy
4.120	0.307	2.397	1.141	-0.382	0.066	-0.262	0.036	0.138	T6.5	SDSS dummy
4.291	0.567	3.006	1.164	-0.399	-0.023	-0.254	0.016	0.103	T7	Gl 229B
4.545	0.618	3.083	0.946	-0.474	-0.259	-0.284	0.031	0.155	T7.5	Gl 570D
4.261	0.582	3.093	1.061	-0.433	-0.152	-0.296	0.034	0.152	T8	2MASS J04151954-0935066

Note: The coordinates of the SDSS objects have been removed, pending acceptance of Chiu et al. (2006, submitted), and will be provided in the published version of the paper.

ject are included in Table 10. The star has $T_{\rm eff}\sim$ 700K (Golimowski et al. 2004), and spectral type T9 (Knapp et al, 2004) in the Geballe et al. (2002) classification scheme, revised to T8 by Burgasser et al. (2006, submitted). Cooler brown dwarfs no doubt exist, but will be difficult to find, because of their very low luminosities. One of the main goals of UKIDSS is to discover such stars. At some temperature a new spectral sequence is expected to appear, possibly associated with the emergence of NH_3 in the spectrum, and the nomenclature Y dwarf has been suggested (Kirkpatrick et al. 1999a, Kirkpatrick 2000). In order to develop a strategy for finding brown dwarfs cooler than $T_{\rm eff}\sim$ 700K we have computed synthetic colours from the model spectra of Burrows, Sudarsky & Lunine (2003), which cover masses in the range $1-10M_{\rm Jup}$, and ages $10^{8.0-9.7}$yr. In Table 11, cols $1-9$ provide predicted colours over the range i to K, col. 10 the K-band absolute magnitude, M_K, and cols $11-14$ list, respectively, the model mass, age, $T_{\rm eff}$, and surface gravity.

Table 12 lists colours computed from similar models by Marley et al. (2002; 2006, in preparation). Cols 1-10 in Table 12 contain the identical information to that for the Burrows et al. models in Table 11, while cols 11 and 12 specify the temperature and surface gravity for the Marley et al. models. These models are for $T_{\rm eff}$ 700 and 600 K, and surface gravities, $\log g$ of 4.48, 5.00 and 5.48 cm s^{-2}, and so sample masses around 15, 30 and 60 $M_{\rm Jup}$ aged $0.4-0.6$, $3.0-4.6$ and $\geqslant 13$ Gyr, respectively. Although the $Y-J$ colours of the Marley models are bluer than the Burrows models, the general trends are similar — very late T and Y dwarfs will have $Y-J$ redder than M dwarfs ($Y-J>0.8$) while $J-H$ will be extremely blue ($J-H<-0.2$).

The synthetic colours for the models of warmer temper-

Table 11. Colours of Burrows et al. (2003) model T and Y cool dwarfs

i–*z*	*Z*–*z*	*Z*–*Y*	*Y*–*J*	*J*–*H*	*H*–*K*	*J*–*J*2	*H*–*H*2	*K*–*K*2	M_K	mass $M_{\rm Jup}$	log *t* yr	$T_{\rm eff}$ K	log *g* cm s^{-2}
4.215	2.247	5.829	2.464	-0.729	0.782	-0.277	0.070	0.100	23.3	1	8.0	290	3.23
8.595	4.556	8.391	4.345	1.175	0.667	-0.323	0.077	0.103	31.3	1	8.5	216	3.27
11.662	6.062	9.928	5.510	2.278	-3.478	-0.377	0.082	0.055	43.5	1	9.0	159	3.32
3.238	1.000	4.193	1.548	-1.018	0.194	-0.272	0.073	0.110	20.0	2	8.0	386	3.53
4.162	2.130	5.626	2.349	-0.529	-0.117	-0.293	0.074	0.105	24.4	2	8.5	283	3.57
8.348	4.314	8.043	4.105	1.325	-1.464	-0.347	0.080	0.109	33.8	2	9.0	208	3.60
12.773	5.796	9.630	6.817	3.962	-2.575	-0.345	0.072	-0.121	45.8	2	9.5	149	3.63
13.659	5.121	8.968	8.828	5.572	-2.164	-0.117	-0.088	-0.514	49.2	2	9.7	134	3.64
4.782	0.612	3.530	1.264	-0.696	0.129	-0.289	0.074	0.133	16.9	5	8.0	588	3.92
4.417	0.835	3.898	1.509	-1.134	-0.448	-0.290	0.078	0.116	19.7	5	8.5	426	3.96
3.338	1.510	4.767	1.879	-0.414	-1.031	-0.302	0.077	0.112	23.7	5	9.0	312	3.99
7.888	3.889	7.526	4.021	1.910	-1.984	-0.350	0.083	0.117	32.5	5	9.5	225	4.02
10.624	5.149	8.955	5.397	3.329	-1.306	-0.357	0.094	0.112	36.7	5	9.7	197	4.03
4.661	0.443	3.062	1.288	-0.454	0.114	-0.292	0.071	0.137	15.8	7	8.0	703	4.07
4.715	0.769	3.778	1.487	-0.833	-0.261	-0.291	0.080	0.125	18.2	7	8.5	507	4.12
2.923	0.888	3.860	1.468	-0.592	-0.998	-0.294	0.078	0.115	21.6	7	9.0	369	4.15
4.418	2.109	5.423	2.318	0.326	-2.213	-0.327	0.078	0.116	27.3	7	9.5	267	4.18
5.737	2.799	6.199	2.905	0.982	-3.279	-0.345	0.078	0.119	30.8	7	9.7	234	4.19
4.190	0.301	2.457	1.409	-0.147	0.092	-0.288	0.074	0.132	14.6	10	8.0	859	4.24
5.044	0.646	3.501	1.398	-0.553	-0.159	-0.292	0.077	0.134	16.8	10	8.5	620	4.29
4.491	0.787	3.733	1.638	-0.892	-0.877	-0.298	0.081	0.120	19.7	10	9.0	447	4.32
3.621	0.690	3.364	1.035	-1.054	-2.160	-0.318	0.076	0.118	24.1	10	9.5	325	4.35
3.848	1.730	4.914	2.042	0.297	-2.128	-0.326	0.078	0.120	26.1	10	9.7	284	4.36
4.924	0.703	3.555	1.546	-0.539	-0.446	-0.294	0.081	0.130	17.3	15	9.0	593	4.52
4.117	0.680	3.448	1.582	-0.854	-1.502	-0.307	0.081	0.122	21.0	15	9.5	414	4.56
2.807	0.802	3.568	1.409	-0.197	-1.903	-0.309	0.080	0.122	22.8	15	9.7	359	4.57
5.172	0.640	3.379	1.475	-0.390	-0.367	-0.293	0.076	0.132	16.3	20	9.0	686	4.66
4.465	0.709	3.493	1.732	-0.661	-1.190	-0.302	0.085	0.125	19.4	20	9.5	483	4.71
4.095	0.642	3.323	1.584	-0.752	-1.671	-0.310	0.083	0.124	21.0	20	9.7	421	4.72
5.107	0.516	3.015	1.452	-0.269	-0.295	-0.290	0.073	0.130	15.4	25	9.0	797	4.80
4.762	0.733	3.517	1.747	-0.517	-0.915	-0.298	0.085	0.126	18.2	25	9.5	555	4.83
4.578	0.698	3.429	1.752	-0.624	-1.344	-0.304	0.086	0.125	19.6	25	9.7	483	4.85

Table 12. Colours of Marley et al. model cool dwarfs

i–*z*	*Z*–*z*	*Z*–*Y*	*Y*–*J*	*J*–*H*	*H*–*K*	*J*–*J*2	*H*–*H*2	*K*–*K*2	M_K	$T_{\rm eff}$ K	log *g* cm s^{-2}
6.027	0.651	3.467	0.849	-1.093	-1.034	-0.294	0.072	0.135	18.2	600	4.48
5.848	0.694	3.359	0.937	-0.919	-1.779	-0.296	0.074	0.131	18.7	600	5.00
5.806	0.730	3.269	0.970	-0.680	-1.762	-0.294	0.073	0.125	18.7	600	5.48
5.908	0.560	3.237	0.942	-0.854	-0.749	-0.289	0.067	0.136	16.9	700	4.48
5.942	0.666	3.287	0.985	-0.786	-1.279	-0.291	0.070	0.129	17.3	700	5.00
5.976	0.779	3.341	1.031	-0.673	-1.402	-0.288	0.068	0.121	17.5	700	5.48

Note: the model spectra extend only to 2.4 μm and the $H-K$ and $K-K2$ colours may be in error by up to 0.02 mag.

ature, which overlap in temperature with the coolest known T dwarfs, are in reasonable agreement with the measured colours of the T dwarfs (Fig. 2), giving some confidence in the synthetic colours of the cooler objects. The range of masses and ages considered give rise to a wide range of predicted colours. The models however all suggest that the coolest brown dwarfs continue getting bluer in the near-infrared with decreasing $T_{\rm eff}$ for $T_{\rm eff} > 400$ K. Burrows, Sudarsky & Lunine (2003) describe the reddening at cooler temperatures to be due to the appearance of water clouds and, more importantly, the collapse of flux on the Wien tail.

Spectral changes occur at temperatures hotter than 400 K: the alkali lines are expected to disappear below 500 K, and at 600 K NH_3 is expected to be detectable at the blue edge of the H and K band peaks (Burrows et al. 2003). The appearance of NH_3 in the near-infrared may signal the next spectral type after T, i.e. Y, as discussed above. WFCAM will allow candidate very late T and Y dwarfs to be identified from their blue $J-H$ colours; these objects will be followed up spectroscopically. The LAS should find several brown dwarfs later than T8 in the first two years of the survey. Adopting a detection limit of $K = 18.4$, the LAS should detect dwarfs as cool as 450 K at 10pc in all YJH bands (col. 10 in Tables 11 and 12). This temperature limit translates to a lower mass limit of 10 Jupiter masses for an assumed age of 1-5 Gyr.

Should young, nearby, even cooler objects be detected in the Y and J bands, Fig. 4 shows that the model $Y-J$ colours are approximately constant with temperature down to 400K, then move rapidly redder. Stellar objects redder than $Y-J = 2$ would be extremely cool, and very interesting objects indeed. Possible contaminants include carbon stars, distinguishable using other colours, and quasars of very–high redshift, $z > 7.8$, which are expected to be extremely rare. Although model colours of elliptical galaxies become very red in $Y-J$ at high redshift $z > 2.8$ (see below), this is only true of an unevolving spectrum. For realistic formation redshifts, such extreme colours would not be seen. For the

model cool brown dwarfs, a similar trend with temperature is seen in the $Z-J$ colour, but a selection limit $Z-J>5$ would be required, which would involve unreasonably long integrations in the Z band. Caution is required however as the model colours are subject to uncertainty, and other authors (Baraffe et al., 2003; Marley, private communication) find somewhat different trends.

5.2.3 Cool white dwarfs

Model spectra of white dwarfs have been provided by P. Bergeron (see e.g. Bergeron et al. 2005, references therein and the web page `http://www.astro.umontreal.ca/~bergeron/CoolingModels/`) and used to calculate colours over the range u to K. The models are for pure H and pure He atmospheres, with surface gravity log$g$ =8. Tables 13 and 14 provide the colours in columns $1-12$, column 13 provides the $K-$band absolute magnitude, and column 14 the effective temperature.

Fig. 2 shows that while He–atmosphere white dwarfs are difficult to distinguish from main sequence stars, hydrogen–rich white dwarfs become blue in $J-H$ at $T_{\rm eff}$ <5000 K. This is due to the onset of pressure–induced molecular hydrogen absorption in these high–pressure atmospheres. White dwarfs can be used as chronometers, as their cooling after the planetary nebula stage is reasonably well understood. The age of the Galactic disk has be constrained by the coolest disk white dwarfs, and if halo white dwarfs can be identified, the age of the halo could also be constrained. This is especially true of the H–rich white dwarfs, as He atmospheres are less opaque and allow the white dwarf to cool rapidly – a He–rich dwarf will be a Gyr or more younger than a H–rich dwarf with the same temperature (e.g. Bergeron, Leggett & Ruiz 2001). Fig. 9 of Bergeron et al. (2005) shows that most white dwarfs known have $T_{\rm eff}$ >4000K and, based on tangential velocity and temperature, are most likely to be (thick) disk dwarfs younger than 10^{10} years. The LAS will be able to detect 4000K H–rich white dwarfs out to around 60 pc, and 3000K H–rich white dwarfs to 20 pc. While these objects are very rare, they occupy a unique region of the $J-H$ *vs* $Y-J$ diagram and will be easy to identify and important to follow-up.

5.3 Galaxies: *hyperz* templates, and the Kinney–Mannucci spectra

We have computed synthetic colours of galaxies over the redshift range $0<z<3.6$, with a step size $\Delta z=0.1$, by redshifting unevolving locally-measured template spectra of different galaxy types. Predictions for the u and g colours at high redshift require the adoption of a model for the effects of intervening absorption. While such a model is employed to make predictions for the quasar SEDs (Section 5.4), galaxy colours at high redshift based on unevolved ultraviolet galaxy SEDs are of limited utility and the u- and g-band simulations are confined to redshifts $z\leqslant 1.7$ and $\leqslant 2.5$ respectively. We have used two published sets of templates, as detailed below.

5.3.1 hyperz templates

The first set of templates are the extended Coleman, Wu & Weedman (1980) spectra that are supplied with and used by the *hyperz* photometric–redshift code (Bolzonella, Miralles & Pelló, 2000). The original Coleman et al. spectra cover the wavelength range $1400<\lambda<10\,000$ Ångstroms, and were extended by Bolzonella et al. to both shorter and longer wavelengths using synthetic spectra created with the GISSEL98 code (Bruzual & Charlot, 1993). The synthetic colours for, respectively, the template E, Sbc, Scd and Im spectra are provided in Tables 15−17. In each table col. 1 lists the redshift, and cols $2-12$ list colours in the u to K bands. Blank entries correspond to redshift ranges where colours would be affected by intergalactic absorption.

The redshift tracks of the $ZYJHK$ colours of the four spectra are plotted in Fig. 3. The effect of redshift is, as a rule, to shift the spectra redward of the locus of stars, i.e. towards the bottom right in each plot. We chose to redshift unevolving templates as this gives an idea of the envelope within which galaxy colours lie at any redshift. But the use of an old stellar population (the E spectrum) to define the red boundary of the colour distribution, becomes unrealistic by redshift $z=2$. Therefore objects discovered in the region of colour space traced by the E spectrum at high redshift, are more likely to be dusty galaxies, not represented by the templates used here.

5.3.2 Kinney–Mannucci spectra

The second set of templates are the spectra created by Mannucci et al. (2001), by combining their near-infrared averaged spectra with the UV–optical template spectra of Kinney et al. (1996). The synthetic colours for, respectively, the template E, S0, Sa, Sb, and Sc spectra are provided in Tables 19−23. In each table col. 1 lists the redshift, and cols $2-12$ list colours in the u to K bands. Blank entries correspond to redshift ranges where colours would be affected by intergalactic absorption or where the template SEDs provide incomplete coverage. The latter restriction is confined to colours involving K at $z=0$ as the spectra of Mannucci et al. (2001) reach only 2.4 μm, where the WFCAM K filter still has significant transmission.

The redshift tracks of the Kinney–Mannucci spectra mostly follow closely the *hyperz* tracks for similar spectral classes.

5.4 Quasars in the redshift range $0<z<8.5$

Given the extended wavelength range covered by the passbands (u through K) and the large redshift range of interest for the quasars, $0<z<8.5$, a quasar SED covering the rest-frame wavelength range $500<\lambda<25\,000$ Ångstroms is required. High signal-to-noise ratio composite spectra from large quasar surveys (Francis et al. 1991; Brotherton et al. 2001; Vanden Berk et al. 2001) provide information for the wavelength range $1000\lesssim\lambda\lesssim 7000$ Ångstroms but additional constraints are needed to model the full wavelength range. The relatively simple model SED employed here has been constructed using the emission line properties of the Large Bright Quasar Survey (LBQS) composite spectrum (Francis et al. 1991) combined with a parametric continuum

Table 13. Colours of pure H atmosphere model white dwarf spectra of different effective temperature

u–*g*	*g*–*r*	*r*–*i*	*i*–*z*	*Z*–*z*	*Z*–*Y*	*Y*–*J*	*J*–*H*	*H*–*K*	*J*–*J*2	*H*–*H*2	*K*–*K*2	M_K	$T_{\rm eff}$ K
1.632	0.932	-2.161	-0.054	-0.147	-1.709	0.832	0.467	-2.569	-0.045	-0.139	-0.036	23.937	1500
1.410	1.204	-1.555	-0.076	-0.124	-1.496	0.747	0.243	-1.871	-0.057	-0.107	-0.032	22.053	1750
1.238	1.334	-1.008	-0.106	-0.105	-1.313	0.668	0.072	-1.341	-0.058	-0.083	-0.033	20.559	2000
1.091	1.391	-0.517	-0.128	-0.091	-1.152	0.587	-0.061	-0.963	-0.054	-0.066	-0.034	19.380	2250
0.962	1.401	-0.092	-0.113	-0.078	-0.998	0.507	-0.154	-0.681	-0.046	-0.051	-0.031	18.390	2500

Note: The full table is published in the electronic version of the paper. A portion is shown here for guidance regarding its form and content.

Table 14. Colours of pure He atmosphere model white dwarf spectra of different effective temperature

u–*g*	*g*–*r*	*r*–*i*	*i*–*z*	*Z*–*z*	*Z*–*Y*	*Y*–*J*	*J*–*H*	*H*–*K*	*J*–*J*2	*H*–*H*2	*K*–*K*2	M_K	$T_{\rm eff}$ K
1.994	2.123	1.111	0.691	0.028	0.394	0.476	0.444	0.316	-0.029	0.013	-0.016	13.858	3500
1.723	1.915	0.975	0.591	0.022	0.326	0.415	0.388	0.276	-0.026	0.011	-0.014	13.710	3750
1.464	1.715	0.851	0.504	0.017	0.268	0.363	0.341	0.243	-0.024	0.010	-0.013	13.583	4000
1.211	1.526	0.741	0.430	0.013	0.219	0.320	0.301	0.216	-0.021	0.009	-0.011	13.471	4250
0.960	1.346	0.645	0.368	0.009	0.178	0.284	0.269	0.192	-0.020	0.008	-0.010	13.373	4500

Note: The full table is published in the electronic version of the paper. A portion is shown here for guidance regarding its form and content.

model. A more complete description of the quasar model SED and the data used to determine the parameters is given in Maddox & Hewett (2006, in preparation) but an outline is given here.

The quasar SED model parameters were defined by requiring the model to reproduce the median colours in $ugrizJ2H2K2$ of a sample of 2708 quasars, magnitudes $i < 17.4$ and redshifts $0.1 \leqslant z \leqslant 3.6$, with unresolved morphologies, from the SDSS DR3 quasar catalogue (Schneider et al. 2005), 90% of which possess 2MASS JHK detections. The "continuum" is represented by a power-law in frequency, $F(\nu) \propto \nu^{\alpha}$ with $\alpha = -0.3$ for $\lambda < 12\,000$ Å and $\alpha = -2.4$ for $\lambda \geqslant 12\,000$ Å. A modest contribution from Balmer continuum radiation is included to model the excess flux needed at ~ 3000 Å. Emission line contributions from the LBQS composite spectrum (Francis et al. 2001) over the wavelength range $1000-6000$ Å are included, along with Hα from an extended version of the LBQS composite, and the addition of a Paschen-α line. The Hα strength in the composite is derived from low-luminosity objects and it is necessary to incorporate a reduction in the equivalent width of Hα as a function of luminosity, i.e. a Baldwin Effect (Baldwin 1977), with a dependence $EW(\mathrm{H}\alpha) \propto L_{qso}^{-0.2}$, to reproduce the behaviour of the median JHK colours as Hα passes through the near-infrared passbands over the redshift range $1 \lesssim z \lesssim 3$.

The effects of intergalactic absorption are incorporated by including the absorption from a Lyman-limit system at 912 Å in the quasar restframe. Absorption due to Lyman-α, β and γ transitions in the Lyman-α forest are included using data from Songaila (2004), which extends to a redshift of $z = 6.5$. At redshift $z = 6.5$ there is almost no flux shortward of 1216 Å and rather than attempting an unconstrained extrapolation of the absorption behaviour to higher redshifts the absorption applicable at $z = 6.5$ has been applied at all redshifts $z > 6.5$. In practice the adoption of the $z = 6.5$ absorption for higher redshifts means that colours involving Z and Y (e.g. $Y-J$) will represent blue limits. However, the amplitude of the discontinuity at 1216 Å is such that such colours are already extremely red (reaching 8 magnitudes) and additional absorption will simply increase the amplitude of the continuum breaks relevant to the detection of quasars at $z > 6.5$.

The simple model quasar SED provides an exceptionally good fit to the median colours, $ugrizJ2H2K2$, over the full redshift range $0.1 \leqslant z \leqslant 3.6$. To provide an indication of the effects of changing the overall shape of the quasar SED on the UKIDSS colours, "blue" and "red" quasar SEDs have been generated by modifying the power-law slope at $\lambda < 12000$ Å to $\alpha = 0.0$ and $\alpha = -0.6$ respectively.

The model colours of the blue, average, and red model quasar spectra, respectively, are provided in Tables 24, 25, and 26, and cover the redshift range $0 < z < 8.5$, with redshift interval $\Delta z = 0.1$. In each table col. 1 lists the redshift, and cols $2-13$ provide colours over the range u to K.

The discovery of quasars of very–high redshift $z > 6$ is another of the key goals of UKIDSS (Warren & Hewett, 2002). The general principle used to find high–redshift quasars $3 < z < 6.4$ with broadband photometry (e.g. Warren, Hewett & Osmer, 1991; Fan et al. 2000b) is to image in three bands, one (a) blueward of redshifted Lyα, a second (b) containing or just redward of Lyα, and a third (c) further to the red. The quasars are then red in $a-b$, and bluer in $b-c$ than any stars, or brown dwarfs, that are similarly red in $a-b$. The most distant quasar found in the SDSS has $z = 6.40$ (Fan et al. 2003; Iwamuro et al. 2004). At higher redshifts Lyα moves out of the z band, and a longer-wavelength middle filter is needed.

Unfortunately in the standard near-infrared bands JHK quasars are redder than most stars (Warren, Hewett & Foltz, 2000), and have similar colours to M stars, late L dwarfs, and early T dwarfs. This means that in a search for quasars of redshift $z > 6.4$ a colour from the JHK bands used as the red colour $b-c$ is not effective. As shown in Fig. 4, the Y band appears to offer a solution. The colour of the average quasar spectrum lies at least 0.5mag. bluer than L and T dwarfs in $Y-J$ until $z \sim 7.2$, so that combining

Table 15. Colours of redshifted *hyperz* E galaxy

z	$u-g$	$g-r$	$r-i$	$i-z$	$Z-z$	$Z-Y$	$Y-J$	$J-H$	$H-K$	$J-J2$	$H-H2$	$K-K2$
0.0	0.766	1.049	0.574	0.484	0.020	0.372	0.404	0.666	0.247	-0.028	0.027	0.017
0.1	0.776	1.263	0.645	0.466	0.037	0.402	0.519	0.607	0.473	-0.025	0.024	-0.021
0.2	0.830	1.628	0.714	0.494	0.014	0.360	0.631	0.572	0.658	-0.043	0.017	-0.009
0.3	1.096	1.935	0.792	0.541	0.025	0.352	0.668	0.658	0.756	-0.038	0.019	-0.023
0.4	1.502	2.054	0.901	0.615	0.027	0.398	0.630	0.756	0.751	-0.044	0.019	-0.060

Note: The full table is published in the electronic version of the paper. A portion is shown here for guidance regarding its form and content.

Table 16. Colours of redshifted *hyperz* Sbc galaxy

z	$u-g$	$g-r$	$r-i$	$i-z$	$Z-z$	$Z-Y$	$Y-J$	$J-H$	$H-K$	$J-J2$	$H-H2$	$K-K2$
0.0	0.102	0.747	0.558	0.495	0.029	0.367	0.382	0.621	0.230	-0.026	0.023	0.018
0.1	0.359	0.848	0.544	0.491	0.030	0.397	0.488	0.579	0.446	-0.024	0.022	-0.017
0.2	0.395	1.051	0.538	0.483	0.029	0.391	0.617	0.548	0.616	-0.039	0.017	-0.010
0.3	0.239	1.290	0.567	0.462	0.029	0.388	0.663	0.621	0.705	-0.040	0.019	-0.024
0.4	0.002	1.520	0.613	0.461	0.029	0.384	0.659	0.730	0.709	-0.038	0.018	-0.053

Note: The full table is published in the electronic version of the paper. A portion is shown here for guidance regarding its form and content.

Table 17. Colours of redshifted *hyperz* Scd galaxy

z	$u-g$	$g-r$	$r-i$	$i-z$	$Z-z$	$Z-Y$	$Y-J$	$J-H$	$H-K$	$J-J2$	$H-H2$	$K-K2$
0.0	-0.072	0.625	0.423	0.328	0.014	0.232	0.367	0.599	0.224	-0.025	0.022	0.018
0.1	0.031	0.738	0.445	0.343	0.015	0.234	0.412	0.561	0.435	-0.023	0.022	-0.016
0.2	-0.030	0.939	0.451	0.352	0.016	0.252	0.453	0.529	0.597	-0.031	0.017	-0.011
0.3	-0.148	1.138	0.466	0.369	0.017	0.262	0.466	0.563	0.681	-0.028	0.018	-0.025
0.4	-0.324	1.268	0.549	0.378	0.017	0.267	0.479	0.597	0.685	-0.030	0.018	-0.050

Note: The full table is published in the electronic version of the paper. A portion is shown here for guidance regarding its form and content.

Table 18. Colours of redshifted *hyperz* Im galaxy

z	$u-g$	$g-r$	$r-i$	$i-z$	$Z-z$	$Z-Y$	$Y-J$	$J-H$	$H-K$	$J-J2$	$H-H2$	$K-K2$
0.0	-0.396	0.423	0.436	0.394	0.020	0.267	0.278	0.503	0.187	-0.019	0.016	0.023
0.1	-0.291	0.509	0.414	0.380	0.022	0.313	0.368	0.477	0.362	-0.019	0.020	-0.012
0.2	-0.372	0.702	0.316	0.366	0.021	0.301	0.498	0.430	0.494	-0.031	0.016	-0.014
0.3	-0.519	0.862	0.274	0.361	0.020	0.289	0.556	0.466	0.569	-0.037	0.014	-0.022
0.4	-0.690	0.907	0.445	0.272	0.018	0.276	0.549	0.569	0.578	-0.034	0.014	-0.035

Note: The full table is published in the electronic version of the paper. A portion is shown here for guidance regarding its form and content.

Table 19. Colours of redshifted Kinney–Mannucci E galaxy

z	$u-g$	$g-r$	$r-i$	$i-z$	$Z-z$	$Z-Y$	$Y-J$	$J-H$	$H-K$	$J-J2$	$H-H2$	$K-K2$
0.0	0.802	1.100	0.605	0.483	0.015	0.340	0.572	0.661	...	-0.035	0.023	...
0.1	1.009	1.312	0.658	0.510	0.031	0.374	0.589	0.718	0.397	-0.034	0.023	-0.022
0.2	1.339	1.659	0.744	0.520	0.024	0.388	0.606	0.769	0.576	-0.038	0.022	-0.007
0.3	1.446	1.981	0.843	0.551	0.034	0.412	0.621	0.822	0.734	-0.034	0.026	-0.017
0.4	1.429	2.171	0.943	0.630	0.022	0.408	0.648	0.844	0.817	-0.040	0.027	-0.050

Note: The full table is published in the electronic version of the paper. A portion is shown here for guidance regarding its form and content.

Table 20. Colours of redshifted Kinney–Mannucci S0 galaxy

z	$u-g$	$g-r$	$r-i$	$i-z$	$Z-z$	$Z-Y$	$Y-J$	$J-H$	$H-K$	$J-J2$	$H-H2$	$K-K2$
0.0	0.728	1.084	0.600	0.471	0.017	0.336	0.551	0.651	...	-0.037	0.023	...
0.1	0.677	1.293	0.653	0.492	0.031	0.377	0.552	0.709	0.433	-0.031	0.022	-0.013
0.2	0.631	1.622	0.733	0.517	0.021	0.370	0.598	0.746	0.606	-0.037	0.021	-0.009
0.3	0.876	1.895	0.833	0.548	0.028	0.389	0.625	0.786	0.739	-0.037	0.026	-0.027
0.4	1.099	1.982	0.928	0.618	0.025	0.411	0.632	0.813	0.805	-0.039	0.026	-0.053

Note: The full table is published in the electronic version of the paper. A portion is shown here for guidance regarding its form and content.

Table 21. Colours of redshifted Kinney–Mannucci Sa galaxy

z	$u-g$	$g-r$	$r-i$	$i-z$	$Z-z$	$Z-Y$	$Y-J$	$J-H$	$H-K$	$J-J2$	$H-H2$	$K-K2$
0.0	0.609	1.080	0.570	0.433	0.021	0.346	0.541	0.673	...	-0.034	0.021	...
0.1	0.687	1.227	0.639	0.475	0.025	0.339	0.570	0.719	0.435	-0.035	0.023	-0.016
0.2	0.661	1.442	0.766	0.480	0.022	0.341	0.601	0.749	0.609	-0.037	0.023	-0.013
0.3	0.719	1.704	0.840	0.536	0.029	0.384	0.582	0.786	0.751	-0.037	0.024	-0.024
0.4	0.633	1.933	0.874	0.633	0.021	0.376	0.594	0.825	0.820	-0.033	0.025	-0.049

Note: The full table is published in the electronic version of the paper. A portion is shown here for guidance regarding its form and content.

Table 22. Colours of redshifted Kinney–Mannucci Sb galaxy

z	$u-g$	$g-r$	$r-i$	$i-z$	$Z-z$	$Z-Y$	$Y-J$	$J-H$	$H-K$	$J-J2$	$H-H2$	$K-K2$
0.0	0.402	0.993	0.577	0.432	0.012	0.292	0.592	0.650	...	-0.038	0.024	...
0.1	0.297	1.129	0.653	0.455	0.025	0.320	0.560	0.726	0.461	-0.033	0.020	-0.017
0.2	0.176	1.371	0.701	0.495	0.023	0.350	0.545	0.792	0.616	-0.035	0.022	-0.012
0.3	0.354	1.566	0.744	0.558	0.024	0.356	0.561	0.823	0.740	-0.030	0.029	-0.029
0.4	0.422	1.639	0.810	0.590	0.024	0.392	0.595	0.802	0.812	-0.037	0.028	-0.053

Note: The full table is published in the electronic version of the paper. A portion is shown here for guidance regarding its form and content.

Table 23. Colours of redshifted Kinney–Mannucci Sc galaxy

z	$u-g$	$g-r$	$r-i$	$i-z$	$Z-z$	$Z-Y$	$Y-J$	$J-H$	$H-K$	$J-J2$	$H-H2$	$K-K2$
0.0	0.101	0.885	0.490	0.424	0.019	0.288	0.555	0.651	...	-0.037	0.023	...
0.1	-0.031	1.040	0.603	0.406	0.023	0.312	0.522	0.721	0.445	-0.031	0.020	-0.017
0.2	-0.007	1.269	0.615	0.411	0.017	0.334	0.534	0.762	0.594	-0.032	0.022	-0.013
0.3	0.151	1.396	0.610	0.536	0.028	0.306	0.557	0.773	0.736	-0.034	0.028	-0.025
0.4	0.309	1.301	0.796	0.511	-0.012	0.302	0.577	0.761	0.813	-0.034	0.026	-0.054

Note: The full table is published in the electronic version of the paper. A portion is shown here for guidance regarding its form and content.

Table 24. Colours of redshifted blue model quasar spectrum

z	$u-g$	$g-r$	$r-i$	$i-z$	$Z-z$	$Z-Y$	$Y-J$	$J-H$	$H-K$	$J-J2$	$H-H2$	$K-K2$
0.0	-1.049	0.470	-0.188	0.130	0.005	0.105	0.418	1.136	1.300	-0.026	0.036	-0.084
0.1	-1.162	0.173	0.634	-0.339	0.008	0.105	0.305	1.001	1.334	-0.019	0.036	-0.076
0.2	-1.181	0.299	0.427	-0.216	0.002	0.056	0.304	0.775	1.358	-0.021	0.036	-0.069
0.3	-1.143	0.301	0.022	0.658	-0.044	-0.504	0.304	0.580	1.290	-0.021	0.029	-0.088
0.4	-1.005	0.141	0.215	0.370	-0.198	-0.411	0.254	0.470	1.204	-0.021	0.017	-0.084

Note: The full table is published in the electronic version of the paper. A portion is shown here for guidance regarding its form and content.

Table 25. Colours of redshifted average model quasar spectrum

z	$u-g$	$g-r$	$r-i$	$i-z$	$Z-z$	$Z-Y$	$Y-J$	$J-H$	$H-K$	$J-J2$	$H-H2$	$K-K2$
0.0	-0.955	0.565	-0.132	0.188	0.009	0.156	0.467	1.137	1.300	-0.028	0.036	-0.084
0.1	-1.069	0.262	0.694	-0.278	0.012	0.156	0.368	1.019	1.334	-0.022	0.036	-0.076
0.2	-1.093	0.389	0.496	-0.164	0.005	0.107	0.367	0.821	1.358	-0.025	0.036	-0.069
0.3	-1.060	0.394	0.084	0.711	-0.041	-0.450	0.366	0.650	1.292	-0.025	0.030	-0.088
0.4	-0.922	0.234	0.275	0.432	-0.197	-0.365	0.317	0.554	1.216	-0.025	0.020	-0.084

Note: The full table is published in the electronic version of the paper. A portion is shown here for guidance regarding its form and content.

Table 26. Colours of redshifted red model quasar spectrum

z	$u-g$	$g-r$	$r-i$	$i-z$	$Z-z$	$Z-Y$	$Y-J$	$J-H$	$H-K$	$J-J2$	$H-H2$	$K-K2$
0.0	-0.862	0.659	-0.075	0.246	0.013	0.207	0.516	1.138	1.300	-0.031	0.036	-0.084
0.1	-0.976	0.350	0.753	-0.217	0.016	0.206	0.430	1.037	1.334	-0.026	0.036	-0.076
0.2	-1.004	0.478	0.566	-0.111	0.009	0.158	0.429	0.868	1.358	-0.028	0.036	-0.069
0.3	-0.976	0.487	0.146	0.763	-0.039	-0.395	0.429	0.721	1.294	-0.028	0.031	-0.088
0.4	-0.839	0.327	0.335	0.493	-0.196	-0.319	0.380	0.638	1.229	-0.028	0.022	-0.085

Note: The full table is published in the electronic version of the paper. A portion is shown here for guidance regarding its form and content.

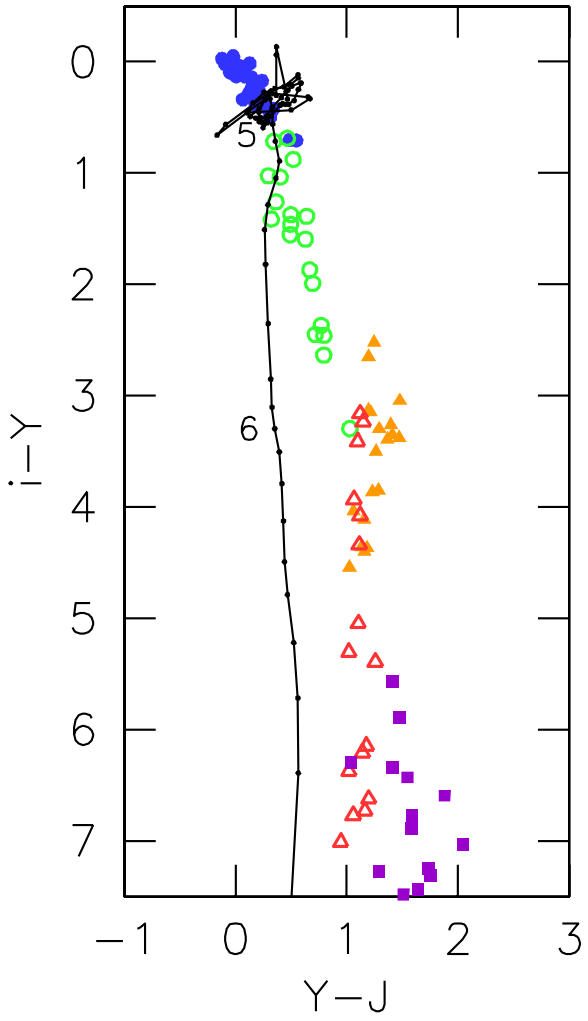

Figure 5. 2–colour diagram illustrating colours of stars, brown dwarfs and quasars. Key: BPGS O–K dwarfs blue ●; M dwarfs green ◯; L dwarfs orange ▲; T dwarfs red △; Burrows model cool brown dwarfs purple ■; quasars $0 < z < 8.5$, $\Delta z = 0.1$, solid black line, with redshifts 5 and 6 marked. In this plot quasars $6 < z < 7.2$ are identifiable as bluer than L and T dwarfs in the $Y - J$ colour. Note that the Marley model cool brown dwarfs all have $i - Y > 7.5$ and so lie off the plot.

UKIDSS data with sufficiently deep $i-$band data it may be possible to discover quasars at redshifts $z > 6.4$.

6 COLOUR EQUATIONS BETWEEN WFCAM, SDSS, AND 2MASS

We have used synthetic colours to compute colour equations relating photometry in the WFCAM bands and the SDSS z and 2MASS $J2$, $H2$, and $K2$ bands i.e. those bands with similar effective wavelengths to WFCAM bands. We used the BPGS atlas, and the additional M stars (Section 5.1.2), but excluded L and T dwarfs which follow different, more complicated, relations. We computed fits for luminosity classes III and V separately. The two fits are mostly similar for any band, but noticeably different in the K band. The following relations allow photometric transformations between the different systems. The root mean square scatter in these relations is 0.01 mag. or less.

$$
\begin{aligned}
Z &= z - 0.01 + 0.051(i - z) && \text{[III]} && (2a)\\
Z &= z - 0.01 + 0.068(i - z) && \text{[V]} && (2b)\\
z &= Z + 0.02 - 0.103(Z - Y) && \text{[III]} && (2c)\\
z &= Z + 0.01 - 0.103(Z - Y) && \text{[V]} && (2d)\\
\\
J &= J2 - 0.01 - 0.003(J2 - H2) && \text{[III]} && (3a)\\
J &= J2 + 0.01 - 0.067(J2 - H2) && \text{[V]} && (3b)\\
J2 &= J + 0.02 && \text{[III]} && (3c)\\
J2 &= J - 0.01 + 0.073(J - H) && \text{[V]} && (3d)\\
\\
H &= H2 + 0.01 + 0.065(H2 - K2) && \text{[III]} && (4a)\\
H &= H2 + 0.080(H2 - K2) && \text{[V]} && (4b)\\
H2 &= H - 0.01 - 0.063(H - K) && \text{[III]} && (4c)\\
H2 &= H - 0.069(H - K) && \text{[V]} && (4d)\\
\\
K &= K2 + 0.075(H2 - K2) && \text{[III]} && (5a)\\
K &= K2 - 0.081(H2 - K2) && \text{[V]} && (5b)\\
K2 &= K - 0.072(H - K) && \text{[III]} && (5c)\\
K2 &= K + 0.073(H - K) && \text{[V]} && (5d)
\end{aligned}
$$

ACKNOWLEDGMENTS

We are grateful to Mark Casali for providing the WFCAM filter transmission curves, to Xiaohui Fan for forwarding the SDSS response functions, to Tom Geballe for providing the ATRAN results, and to Pierre Bergeron for the model cool white dwarf spectra used here.

REFERENCES

Baldwin J. A., 1977, ApJ, 214, 679
Baraffe I., Chabrier G., Barman T. S., Allard F., Hauschildt P. H., 2003, A&A, 402, 701
Bergeron P., Ruiz M. T., Hamuy M., Leggett S. K., Currie M. J., Lajoie C.-P., Dufour P., 2005, ApJ, 625, 838
Bohlin R. C., Gilliland R. L., 2004, AJ, 127, 3508
Bolzonella M., Miralles J.-M., Pelló R., 2000, A&A, 363, 476
Brotherton M. S., Tran H. D., Becker R. H., Gregg M. D., Laurent-Muehleisen S. A., White R. L., 2001, ApJ, 546, 775
Bruzual A. G., Charlot S., 1993, ApJ, 405, 538
Burgasser A. J., et al., 2002, ApJ, 564, 421
Burgasser A. J., Kirkpatrick J. D., Liebert J., Burrows A., 2003, ApJ, 594, 510
Burrows A., Sudarsky D., Lunine J. I., 2003, ApJ, 596, 587
Cohen M., Wheaton W. A., Megeath S. T., 2003, AJ, 126, 1090
Coleman G. D., Wu C.-C., Weedman D. W., 1980, ApJS, 43, 393
Cruz K. L., Reid I. N., Liebert J., Kirkpatrick J. D., Lowrance P. J., 2003, AJ, 126, 2421
Cutri R. M., Skrutskie M. F., Van Dyk S., et al., 2003, Explanatory Supplement to the 2MASS All Sky Data Release, IPAC

Dahn C. C., et al., 2002, AJ, 124, 1170
Dalton G. B., et al., 2004, SPIE, 5492, 988
ESA, 1997, The Hipparcos and Tycho Catalogues, ESA Publ. 1239
Fan X., et al., 2000a, AJ, 119, 928
Fan X., et al., 2000b, AJ, 120, 1167
Fan X., et al., 2003, AJ, 125, 1649
Francis P. J., Hewett P. C., Foltz C. B., Chaffee F. H., Weymann R. J., Morris S. L., 1991, ApJ, 373, 465
Fukugita M., Ichikawa T., Gunn J. E., Doi M., Shimasaku K., Schneider D. P., 1996, AJ, 111, 1748
Geballe T. R., Kulkarni S. R., Woodward C. E., Sloan G. C., 1996, ApJ, 467, L101
Geballe T. R., Saumon D., Leggett S. K., Knapp G. R., Marley M. S., Lodders K., 2001, ApJ, 556, 373
Geballe T. R., et al., 2002, ApJ, 564, 466
Golimowski D. A., et al., 2004, AJ, 127, 3516
Gunn J. E., Stryker L. L., 1983, ApJS, 52, 121
Hass G., Hadley L., 1963, in D. E. Gray, ed., American Institute of Physics Handbook, 2nd Edition, McGraw-Hill, New York, p. 6
Hawarden T. G., Leggett S. K., Letawsky M. B., Ballantyne D. R., Casali M. M., 2001, MNRAS, 325, 563
Hawley S. L., Gizis J. E., Reid I. N., 1996, AJ, 112, 2799
Hayes D. S., Latham D. W., 1975, ApJ, 197, 593
Henry T. J., Kirkpatrick J. D., Simons D. A., 1994, AJ, 108, 1437
Hillenbrand L. A., Foster J. B., Persson S. E., Matthews K., 2002, PASP, 114, 708
Kinney A. L., Calzetti D., Bohlin R. C., McQuade K., Storchi-Bergmann T., Schmitt H. R., 1996, ApJ, 467, 38
Kirkpatrick J. D., Henry T. J., Simons D. A., 1995, AJ, 109, 797
Kirkpatrick J. D., Beichman C. A., Skrutskie M. F., 1997, ApJ, 476, 311
Kirkpatrick J. D., et al., 1999a, ApJ, 519, 802
Kirkpatrick J. D., Allard F., Bida T., Zuckerman B., Becklin E. E., Chabrier G., Baraffe I., 1999b, ApJ, 519, 834
Kirkpatrick J. D., 2000, ASPC, 212, 20
Kirkpatrick J. D., et al., 2000, AJ, 120, 447
Kirkpatrick J. D., 2003, IAUS, 211, 497
Knapp G. R., et al., 2004, AJ, 127, 3553
Leggett S. K., Allard F., Dahn C., Hauschildt P. H., Kerr T. H., Rayner J., 2000a, ApJ, 535, 965
Leggett S. K., et al., 2000b, ApJ, 536, L35
Leggett S. K., Allard F., Geballe T. R., Hauschildt P. H., Schweitzer A., 2001, ApJ, 548, 908
Leggett S. K., Hauschildt P. H., Allard F., Geballe T. R., Baron E., 2002a, MNRAS, 332, 78
Leggett S. K., et al., 2002b, ApJ, 564, 452
Liebert J., Reid I. N., Burrows A., Burgasser A. J., Kirkpatrick J. D., Gizis J. E., 2000, ApJ, 533, L155
Lord S. D. 1992, NASA Technical Memorandum, 103957
McLean I. S., McGovern M. R., Burgasser A. J., Kirkpatrick J. D., Prato L., Kim S. S., 2003, ApJ, 596, 561
Mannucci F., Basile F., Poggianti B. M., Cimatti A., Daddi E., Pozzetti L., Vanzi L., 2001, MNRAS, 326, 745
Marley M. S., Seager S., Saumon D., Lodders K., Ackerman A. S., Freedman R. S., Fan X., 2002, ApJ, 568, 335
Oke J. B., Gunn J. E., 1983, ApJ, 266, 713
Puget P., et al., 2004, SPIE, 5492, 978
Reid I. N., Hawley S. L., Gizis J. E., 1995, AJ, 110, 1838
Reid I. N., Burgasser A. J., Cruz K. L., Kirkpatrick J. D., Gizis J. E., 2001, AJ, 121, 1710
Schneider D. P., et al., 2005, AJ, 130, 367
Schneider D. P., Gunn J. E., Hoessel J. G., 1983, ApJ, 264, 337
Schultz A. B., et al., 1998, ApJ, 492, L181
Simons D. A., Tokunaga A., 2002, PASP, 114, 169
Smith J. A., et al., 2002, AJ, 123, 2121
Songaila A., 2004, AJ, 127, 2598
Strauss M. A., et al., 1999, ApJ, 522, L61
Strecker D. W., Erickson E. F., Witteborn F. C., 1979, ApJS, 41, 501
Tinney C. G., Burgasser A. J., Kirkpatrick J. D., 2003, AJ, 126, 975
Tinney C. G., Delfosse X., Forveille T., Allard F., 1998, A&A, 338, 1066
Tokunaga A. T., Simons D. A., Vacca W. D., 2002, PASP, 114, 180
Tokunaga A. T., Vacca W. D., 2005, PASP, 117, 421
Tsvetanov Z. I., et al., 2000, ApJ, 531, L61
Vanden Berk D. E., et al., 2001, AJ, 122, 549
Vrba F. J., et al., 2004, AJ, 127, 2948
York D. G., et al., 2000, AJ, 120, 1579
Warren S., Hewett P., 2002, ASPC, 283, 369
Warren S. J., Hewett P. C., Foltz C. B., 2000, MNRAS, 312, 827
Warren S. J., Hewett P. C., Osmer P. S., 1991, ApJS, 76, 23